Atmospheric correction of ocean color imagery: use of the Junge power-law aerosol size distribution with variable refractive index to handle aerosol absorption

Roman M. Chomko and Howard R. Gordon

When strongly absorbing aerosols are present in the atmosphere, the usual two-step procedure of processing ocean color data—(1) atmospheric correction to provide the water-leaving reflectance (ρ_w), followed by (2) relating ρ_w to the water constituents—fails and simultaneous estimation of the ocean and aerosol optical properties is necessary. We explore the efficacy of using a simple model of the aerosol—a Junge power-law size distribution consisting of homogeneous spheres with arbitrary refractive index—in a nonlinear optimization procedure for estimating the relevant oceanic and atmospheric parameters for case 1 waters. Using simulated test data generated from more realistic aerosol size distributions (sums of log-normally distributed components with different compositions), we show that the ocean's pigment concentration (C) can be retrieved with good accuracy in the presence of weakly or strongly absorbing aerosols. However, because of significant differences in the scattering phase functions for the test and power-law distributions, large error is possible in the estimate of the aerosol optical thickness. The positive result for C suggests that the detailed shape of the aerosol-scattering phase function is not relevant to the atmospheric correction of ocean color sensors. The relevant parameters are the aerosol single-scattering albedo and the spectral variation of the aerosol optical depth. We argue that the assumption of aerosol sphericity should not restrict the validity of the algorithm and suggest an avenue for including colored aerosols, e.g., wind-blown dust, in the procedure. A significant advantage of the new approach is that realistic multicomponent aerosol models are not required for the retrieval of C.

OCIS codes: 010.0010, 010.1110, 010.1310, 010.4450, 330.1690.

1. Introduction

It is now generally recognized that measurement of the radiance reflected from the ocean atmosphere system can be used to estimate the concentration of phytoplankton pigments, the sum of the concentrations of chlorophyll *a* and phaeophytin *a*, in the ocean.[1–3] (At present, this estimation is generally limited to case 1 waters,[3] i.e., waters in which phytoplankton and their immediate detrital material constitute the variable component of the water's optical properties.) Thus several sensors have been, or are soon to be, launched for the purpose of studying the spatial–temporal variation of phytoplankton globally to understand the role of phytoplankton and their variability in global climate. The sea-viewing wide field-of-view sensor[4] (SeaWiFS) was launched on 1 August 1997, and the moderate-resolution imaging spectroradiometer[5] (MODIS) is scheduled for launch in the summer of 1998. In case 1 waters, the component of the measured radiance that carries information about the phytoplankton concentration, the radiance backscattered out of the water and transmitted to the top of the atmosphere (TOA) (the water-leaving radiance), is at most 10% in the blue and typically much smaller in the green. The rest of the signal is comprised of radiance reflected from the atmosphere and the sea surface. Thus the water-leaving radiance must be extracted from the measured radiance—a process referred to as atmospheric correction.

Typically, atmospheric correction algorithms assume that radiative transfer in the ocean and atmosphere can be decoupled, i.e., photons are never backscattered out of the ocean more than once.[6] Furthermore, determination of the phytoplankton pigment concentration is carried out in two steps:

The authors are with the Department of Physics, University of Miami, Coral Gables, Florida 33124.

Received 6 January 1998; revised manuscript received 10 April 1998.

0003-6935/98/245560-13$15.00/0

(1) the water-leaving radiance is retrieved as a product of the atmospheric correction and (2) the pigment concentration is determined from the water-leaving radiance. The atmospheric correction algorithm has increased in complexity from the simple single-scattering algorithm[7,8] used for the Coastal Zone Color Scanner (CZCS)—the proof-of-concept ocean color mission—to the complete multiple-scattering algorithm proposed for SeaWiFS.[9,10] The new algorithm is capable of providing the water-leaving radiance with the required accuracy for typical marine atmospheres; however, it fails when the atmosphere contains strongly absorbing aerosols, e.g., in the presence of urban pollution or desert dust transported over the ocean by the winds.

Recently, Gordon *et al.*[11] proposed an algorithm for case 1 waters that is capable of atmospheric correction in the presence of both weakly and strongly absorbing aerosols. In this algorithm, the aerosol properties and the pigment concentration are determined simultaneously. This simultaneous determination is required because the aerosol absorption is manifest mostly in the blue, where the water-leaving radiance is usually largest and the most variable. In effect, in this algorithm the ocean pigment concentration and the aerosol model are systematically varied and the TOA radiance is computed. The candidate aerosol models used in this algorithm were derived from the bimodal log-normal aerosol size distributions and refractive indices provided by Shettle and Fenn[12] as a function of relative humidity. The water-leaving radiance was computed as a function of the pigment concentration (C) and a marine particulate scattering factor (b^0) by use of the semianalytic model of Gordon *et al.*[13] The mean of the ocean–atmosphere properties that yield the ten best fits (in a rms sense) of the computed to the measured radiances provides the derived parameters (pigment concentration, aerosol optical thickness, aerosol single-scattering albedo, etc.).

Zhao and Nakajima[14] proposed a similar algorithm for the CZCS, i.e., the aerosol properties and the pigment concentration are determined simultaneously; however, because of the severe limitation of the number of spectral bands on the CZCS, they employed models with Junge[15] power-law size distributions with a single index of refraction and used ratios of water-leaving radiances rather than the water-leaving radiance itself. They showed good retrievals with simulated test data created by use of bimodal aerosol size distributions with the same index of refraction as the Junge power-law distribution and concluded that the power-law distribution was an adequate approximation to the now favored bimodal aerosol distributions for the purposes of atmospheric correction. In contrast to bimodal log-normal size distributions, which require several parameters to describe (the modal diameters and standard deviations of both modes along with their relative concentrations), the simplicity of the Junge power-law distribution is attractive in that only one parameter is required. A further simplification is that the bimodal distributions require an index of refraction for each mode (typically different), whereas a single refractive index is usually assumed for the power-law distribution.

In this paper we explore replacing the Shettle and Fenn[12] candidate aerosol bimodal models in the Gordon *et al.*[11] procedure with a Junge power-law model; however, to be able to deal with both weakly and strongly absorbing aerosols, we let the real and imaginary parts of the index of refraction vary as well as the size distribution parameter—a natural extension of the Zhao–Nakajima[14] algorithm. Thus all the properties of the aerosol are allowed to vary continuously, subject to the constraint of the given mathematical form for the aerosol size distribution. This allows use of nonlinear optimization techniques to effect a solution. The results show that excellent retrievals of the pigment concentration are obtained, weakly and strongly absorbing aerosols are easily identified, but the retrieved aerosol optical thickness can have large errors because of the significant differences in the scattering phase functions for bimodal log-normal and power-law distributions. Thus we also answer the question, is a correct aerosol phase function really required for atmospheric correction of ocean color imagery?

We begin with a description of the aerosol and ocean models used in the procedure and describe the nonlinear optimization. Next we provide tests with simulated data that are free of radiometric calibration errors and follow with an examination of the effect of realistic radiometric calibration errors. Finally, we examine the performance of the algorithm as a function of the aerosol's vertical distribution.

2. Correction Mechanics

We begin by using a generalized reflectance ρ in place of radiance L. These are related by $\rho = \pi L/F_0 \cos\theta_0$, where F_0 is the extraterrestrial solar irradiance and θ_0 is the solar zenith angle. Then, after avoiding Sun glitter and correcting for the presence of whitecaps, the remaining upwelling reflectance at the TOA $\rho_t(\lambda)$ consists of the following components[10]: the pure Rayleigh- (molecular) scattering contribution $\rho_r(\lambda)$, the pure aerosol-scattering contribution $\rho_a(\lambda)$, the contribution that is due to the interaction effect between air molecules and aerosols $\rho_{ra}(\lambda)$, and the desired water-leaving contribution $t(\lambda)\rho_w(\lambda)$, i.e.,

$$\rho_t(\lambda) = \rho_r(\lambda) + \rho_a(\lambda) + \rho_{ra}(\lambda) + t(\lambda)\rho_w(\lambda), \qquad (1)$$

where $t(\lambda)$ is the diffuse transmittance of the atmosphere. As $\rho_r(\lambda)$ can be computed precisely from an estimate of the surface atmospheric pressure,[16,17] it can be subtracted from $\rho_t(\lambda)$ to form

$$[\rho_t(\lambda) - \rho_r(\lambda)] = [\rho_a(\lambda) + \rho_{ra}(\lambda)] + [t(\lambda)\rho_w(\lambda)]. \qquad (2)$$

Following Gordon *et al.*[11] we use an atmospheric model to compute $\rho_a(\lambda) + \rho_{ra}(\lambda)$ and $t(\lambda)$, an ocean model to compute $\rho_w(\lambda)$, and compare the results to the given value of $\rho_t(\lambda) - \rho_r(\lambda)$.

A. Water and Aerosol Models

The water reflectance model is derived from Gordon *et al.*[13] and is identical to that employed by Gordon *et al.*[11] It has two parameters C, the pigment concentration, and b^0, a parameter related to particulate scattering.[3] The model assumes that the upwelling spectral radiance below the sea surface is totally diffuse, contrary to the observations of Morel and coworkers.[18–21] However, as Morel and Gentili[21] have shown, bidirectional effects can be easily introduced into the model and described as a function of C (and, if necessary, b^0).

The aerosol model utilizes a Junge power-law size distribution:

$$\begin{aligned}\frac{dN}{dD} &= K, && D_0 < D \le D_1,\\ &= K\left(\frac{D_1}{D}\right)^{\nu+1}, && D_1 < D \le D_2,\\ &= 0, && D > D_2,\end{aligned}$$

where dN is the number of particles per unit volume with diameters between D and $D + dD$. In this paper we choose $D_0 = 0.06$ μm, $D_1 = 0.20$ μm, and $D_2 = 20$ μm. The size distribution is thus characterized by a single parameter ν. A refractive index $m = m_r - im_i$ is then combined with this size distribution to compute the aerosol optical properties—the phase function, optical thickness $[\tau_a(\lambda)]$, and single-scattering albedo $[\omega_0(\lambda)]$—by use of Mie theory. As the synthetic test data are also computed from bimodal aerosol models with Mie theory (Subsection 3.A), this procedure does not introduce any error, i.e., we assume that all particles are spherical. The aerosol optical properties are then used to generate the reflectance $\rho_a(\lambda) + \rho_{ra}(\lambda)$ as a function of the aerosol optical thickness for all Sun-viewing geometries. A two-layer radiative transfer code (aerosols in the lower layer) in which the air–sea interface is modeled by a flat Fresnel-reflecting surface is used in the computations. These reflectances are stored in the form of lookup tables (LUT's) for rapid access by the algorithm. In our LUT's, the values of the parameter ν range from 2 to 4.5 in steps of 0.5, and $m_i = 0$, 0.001, 0.003, 0.01, 0.03, and 0.04, with $m_r = 1.333$ and 1.50. Thus we have a total of 72 distinct power-law aerosol models that can be used to interpolate for arbitrary values of ν, m_r, and m_i. We use linear interpolation for ν and quadratic interpolation for m_r and m_i (Formula 25.2.66 of Ref. 22).

In the optimization procedure, there are a total of six parameters: C and b^0 for the water and ν, m_r, m_i, and $\tau_a(865)$, for the atmosphere. [The aerosol optical thickness at 865 nm, $\tau_a(865)$, is the measure of the aerosol concentration.] However, we can reduce the number of parameters by noting that $\rho_w \approx 0$ in the near infrared (NIR). (SeaWiFS has NIR bands at 765 and 865 nm, whereas MODIS has bands at 748 and 869 nm.) For these bands, the value of $\rho_a(\lambda) + \rho_{ra}(\lambda)$ is known. The spectral variation of $\rho_a(\lambda) + \rho_{ra}(\lambda)$ in the NIR has been shown to depend mostly on the aerosol size distribution and only slightly on the refractive index,[10] thus these two bands can be used to determine the size distribution parameter ν. This is effected by comparing the measured value of

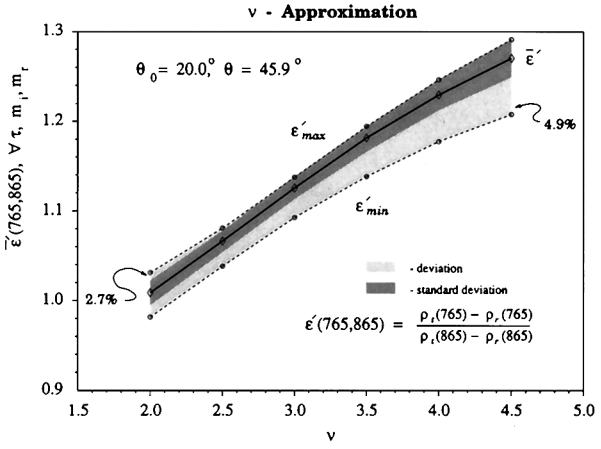

Fig. 1. Relationship between $\varepsilon'(765, 865)$ and ν (solid curve) averaged over all combinations of four values of $\tau_a(865)$ (0.1, 0.2, 0.3, *and* 0.4), six values of m_i (0, 0.001, 0.003, 0.01, 0.03, and 0.04), and two values of m_r (1.333 and 1.50), with $\theta_0 = 20°$ and $\theta = 45.9°$. Dashed curves represent the upper and lower envelopes of the relationship, and the darker area represents the standard deviation of the various cases about the mean for the given value of ν.

$$\varepsilon'(\lambda_s, \lambda_\ell) = \frac{\rho_a(\lambda_s) + \rho_{ra}(\lambda_s)}{\rho_a(\lambda_\ell) + \rho_{ra}(\lambda_\ell)}, \tag{3}$$

where λ_s and λ_ℓ are the shorter and the longer of the two NIR bands available on the sensor, with that computed from the models as a function of ν. Figure 1 shows an example of the relationship between ν and $\varepsilon'(765, 865)$ for the power-law distributions. Figure 1 was prepared with the 12 values of the complex refractive index and four values of $\tau_a(865)$. It shows that a coarse estimate of ν (maximum error $\sim +0.3$ to -0.1, standard error $\sim +0.15$ to -0.1) can be obtained from the measured $\varepsilon'(765, 865)$. Given the value of ν determined from the ν–$\varepsilon'(765, 865)$ relationship for the given geometry, it is a simple matter to compute the aerosol optical thickness that provides the correct value of reflectance at λ for each $m_r - im_i$. Thus both ν and $\tau_a(865)$ can be removed from the list of unknown parameters with the NIR measurements. In the case of SeaWiFS, this leaves six bands from which the four remaining parameters must be determined. It should be noted that use of this method of reducing the number of parameters introduces some error. For example, if the actual aerosol model is identical to one of the 72 candidate models, a close, but incorrect, value of ν will usually be chosen by the algorithm.

B. Nonlinear Optimization

Before continuing the discussion we introduce some simplifying notations:

$$\begin{aligned}\rho_A'(\lambda_j; m_i, m_r) &\equiv \rho_a(\lambda_j; m_i, m_r) + \rho_{ra}(\lambda_j, m_i, m_r),\\ \rho_W'(\lambda_j; C, b^0) &\equiv t(\lambda_j)\rho_w(\lambda_j; C, b^0),\end{aligned} \tag{4}$$

where ρ'_A is the resulting reflectance of the aerosol and interaction term computed at λ_j for the Junge power-law size distribution with the parameters ν and $\tau_a(865)$ (both determined as in Subsection 2.A) by use of m_i and m_r, and ρ_W' is the diffusely transmitted normalized water-leaving reflectance computed at λ_j for water parameters C and b^0. The assumption that $\rho_A'(\lambda_j; m_i, m_r)$ and $\rho_W'(\lambda_j; C, b^0)$ form the final reflectance field on the TOA independently leads to the system of nonlinear equations in four variables (m_i, m_r, C, b^0):

$$\begin{aligned}
\rho_A'(\lambda_1; m_i, m_r) + \rho_W'(\lambda_1; C, b^0) &= \rho_t(\lambda_1) - \rho_r(\lambda_1),\\
\rho_A'(\lambda_2; m_i, m_r) + \rho_W'(\lambda_2; C, b^0) &= \rho_t(\lambda_2) - \rho_r(\lambda_2),\\
&\cdots\cdots\cdots\cdots\\
\rho_A'(\lambda_{N_v}; m_i, m_r) + \rho_W'(\lambda_{N_v}; C, b^0) &= \rho_t(\lambda_{N_v}) - \rho_r(\lambda_{N_v}).
\end{aligned} \tag{5}$$

We seek to solve this set of equations for m_i, m_r, C, and b^0 when N_v, the number of visible bands used in the retrieval, is greater than the number of unknowns in Eqs. (4) and adopt a nonlinear optimization procedure to do so. We note that the set of variables (m_i, m_r, C, b^0) is subject to the following constraints:

$$\begin{aligned}
&0 \le m_i(\min) \le m_i \le m_i(\max),\\
&0 < m_r(\min) \le m_r \le \ \le m_r(\max),\\
&0 < C(\min) \le C \le C(\max),\\
&0 < b^0(\min) \le b^0 \le b^0(\max).
\end{aligned} \tag{6}$$

As in Gordon *et al.*,[11] we assume that $C(\min) = 0.05$ mg/m^3, $C(\max) = 1.50$ mg/m^3, $b^0(\min) = 0.12$ m^{-1}, and $b^0(\max) = 0.45$ m^{-1}. For the atmosphere, we take $m_i(\min) = 0$, $m_i(\max) = 0.04$, $m_r(\min) = 1.33$, and $m_r(\max) = 1.50$ as realistic ranges for the aerosol parameters. We choose as the least-squares (LSQ) objective function

$$S_{\mathrm{LSQ}}{}^2(m_i, m_r, C, b^0) = \frac{1}{(N_v - 1)} \times \sum_{i=1}^{N_v} \left[\frac{\rho_A'(\lambda_j; m_i, m_r) + \rho_W'(\lambda_j; C, b^0)}{\rho_t(\lambda_j) - \rho_r(\lambda_j)} - 1 \right]^2. \tag{7}$$

At the solution point $(m_i{}^*, m_r{}^*, C^*, b^{0*})$, S_{LSQ} should attain its minimal value subject to constraints in inequalities (6).

A number of versatile methods exist to find such a solution,[23] although they might differ appreciably as to the convergence rate, the memory requirements, and the ability to converge to the solution. In particular, methods belonging to the so-called quasi-Newton class[24] that take advantage of the information contained in the Hessian matrix of a function (i.e., the square matrix of the second partial derivatives of the function evaluated at a point) in calculating the step size and the direction of search appear to be adequate for our purposes. Powell[25] proves the convergence to a minimum for the Davidon–Fletcher–Powell variable metric class method [which also holds for Broyden–Fletcher–Goldfarb–Shanno algorithm] on a function with properties outlined above [Eqs. (5) and inequalities (6)]. However, to the best of our knowledge, the quasi-Newton class methods do not guarantee, in general, a convergence to a minimum. In this study we used the DZXMWD routine from the commonly available International Mathematical & Statistical Library,[26] which is based on the Harwell Library routine VA10A and incorporates a quasi-Newton method. To assure the convergence to a minimum in our nonlinear optimization procedure a set of starting search points is taken, some of which are discarded after performing a few iterations based on their relative values. We observed that the resulting solution was the same (within a preset tolerance) whatever the number of starting search points chosen, meaning that convergence to a global minimum was probably achieved, so we believe it is sufficient to use just one starting point in solving the system [Eqs. (5)], and the result is the solution we want.

3. Algorithm Performance with Simulated Data

A. Characteristics of the Simulated $\rho_t(\lambda)$ Data

As in earlier research,[9,11] we tested the performance of the algorithm with simulated data—pseudodata. The pseudodata were created by choosing specific values of C and b^0 for the computation of $\rho_w(\lambda)$ and by utilizing specific aerosol models for the computation of $\rho_r + \rho_a + \rho_{ra}$. The aerosol models we chose for the tests were those developed by Shettle and Fenn[12] at a relative humidity of 80%. For these the size frequency distribution is written as

$$\frac{\mathrm{d}N}{\mathrm{d}D} = \sum_{i=1}^{M} \frac{\mathrm{d}N_i}{\mathrm{d}D}, \tag{8}$$

where $\mathrm{d}N_i$ is the number of particles per unit volume with diameters between D and $D + \mathrm{d}D$ of the ith species or component. The individual components are taken to be log-normally distributed[12]:

$$\frac{\mathrm{d}N_i}{\mathrm{d}D} = \frac{N_i}{\log_e(10)\sqrt{2\pi}\sigma_i D} \exp\left\{ -\frac{1}{2}\left[\frac{\log_{10}(D/D_i)}{\sigma_i} \right] \right\}, \tag{9}$$

where D_i and σ_i are the modal diameter and the standard deviation, respectively, and N_i is the total number density of the ith component. Table 1 provides the parameters N_i, D_i, σ_i, and $m_r - im_i$ for each test aerosol model. The nomenclature M80, C80, T80, and U80 refers to the maritime, coastal, tropospheric, and urban aerosol models[12] at 80% relative humidity. Figure 2 provides the spectral variation in τ_a for the four test aerosol models. Note that the spectral variation of the test data is enclosed within the range of the candidate aerosol set for which $\tau_a(\lambda)/\tau_a(865) \approx (865/\lambda)^{(\nu-2)}$. To provide a sense of how well the candidate size distribution approximates the test distributions, Fig. 3 compares the volume size

Table 1. Characteristics of the Test Aerosol Models used in the Study

Aerosol Model	Size Distribution			Refractive Index	
	N_i	D_i	σ_i	412 nm	865 nm
M80	0.990000	0.06548	0.35	1.446-*i*3.309*E*-3	1.436-*i*6.107*E*-3
	0.010000	0.63600	0.40	1.359-*i*5.165*E*-9	1.348-*i*1.381*E*-6
C80	0.995000	0.06548	0.35	1.446-*i*3.309*E*-3	1.436-*i*6.107*E*-3
	0.005000	0.63600	0.40	1.359-*i*5.165*E*-9	1.348-*i*1.381*E*-6
T80	1.000000	0.06548	0.35	1.446-*i*3.309*E*-3	1.436-*i*6.107*E*-3
U80	0.999875	0.07028	0.35	1.423-*i*3.473*E*-2	1.414-*i*3.412*E*-2
	0.000125	1.16200	0.40	1.415-*i*3.151*E*-2	1.406-*i*3.095*E*-2

distribution $dV/d\ln D$ of three of the four test models (solid curves) with that for the Junge power-law distribution (dotted curves). In Fig. 3, all volume distributions are normalized such that $\int_0^\infty dN = 1$. Because of their bimodality, M80 and U80 can be better represented by Junge power-law distributions than T80. Table 2 provides the single-scattering albedo for the test models. Clearly, U80 absorbs much more strongly than the others, which we refer to as weakly absorbing.

A test data set was simulated by computing $\rho_t(\lambda) - t(\lambda)\rho_w(\lambda)$ for the M80, C80, T80, and U80 aerosol models with $\tau_a(865) = 0.1$, 0.2, and 0.3, $\rho_w(\lambda)$ with $b^0 = 0.3\ m^{-1}$ (the adopted mean value[3] for case 1 waters) and $C = 0.1$, 0.5, and 1.0 mg/m^3. Note that for the test data, the aerosol optical thickness at 412 nm can be as high as 0.80 for T80 (Fig. 2). The simulated data were created for solar zenith angles (θ_0) of 0°, 20°, 40°, and 60°, with the sensor viewing at an angles (θ) of ≈1° and ≈45° with respect to nadir and an azimuth (ϕ) of 90° relative to the Sun. These cover much of the Sun-viewing geometry available to an ocean color sensor. The combination $\theta_0 = 0$ and $\theta \approx 1°$ is excluded, as it would be within the Sun's glitter pattern, so there are a total of seven Sun-viewing geometries considered.

B. Retrieval Results for Error-Free ρ_t

In this subsection we examine the performance of the algorithm when the TOA reflectance ρ_t is free of error. Examples of the retrieval of the spectra of $\rho_a + \rho_{ra}$ and $t\rho_w$, along with the true values and the recovered values of the parameters, are provided in Fig. 4 for two different Sun-viewing geometries and pseudodata generated with two different aerosol models (M80 and U80). The retrievals were effected by use of the first five SeaWiFS bands (412, 443, 490, 510, and 555 nm) in the nonlinear optimization and 765 and 865 nm to determine ν and $\tau_a(865)$. The results indicate excellent fits between the measured and reconstructed values of $\rho_t(\lambda) - \rho_r(\lambda)$ that are obtained for both the strongly (U80) and the weakly (M80) absorbing aerosols. The retrieved $t\rho_w(\lambda)$ is also ex-

Table 2. Values of Single-Scattering Albedo at λ = 412 and 865 nm for the Test Aerosol Models used in the Study

Aerosol Model	λ (nm)	ω_0
M80	412	0.992387
	865	0.993423
C80	412	0.988392
	865	0.988439
T80	412	0.975839
	865	0.952837
U80	412	0.782303
	865	0.748059

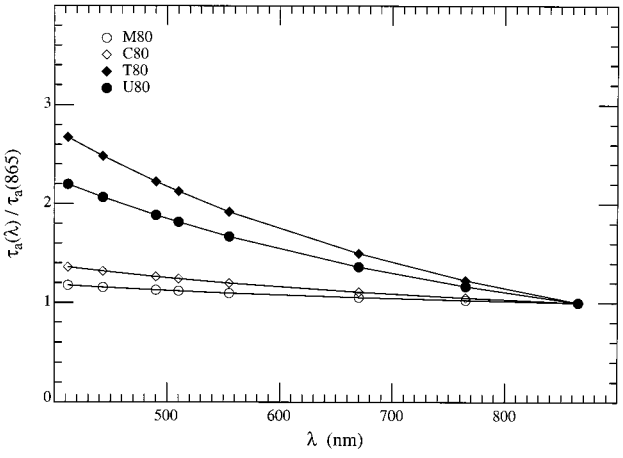

Fig. 2. Spectral variation of the aerosol optical thickness for the models used to generate the test pseudodata.

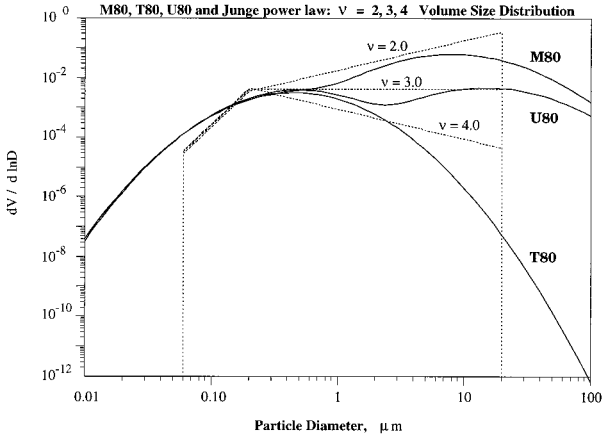

Fig. 3. Comparison between the volume size distribution of the aerosol models used to generate the test pseudodata (solid curves) and the Junge power-law distribution (dotted curves).

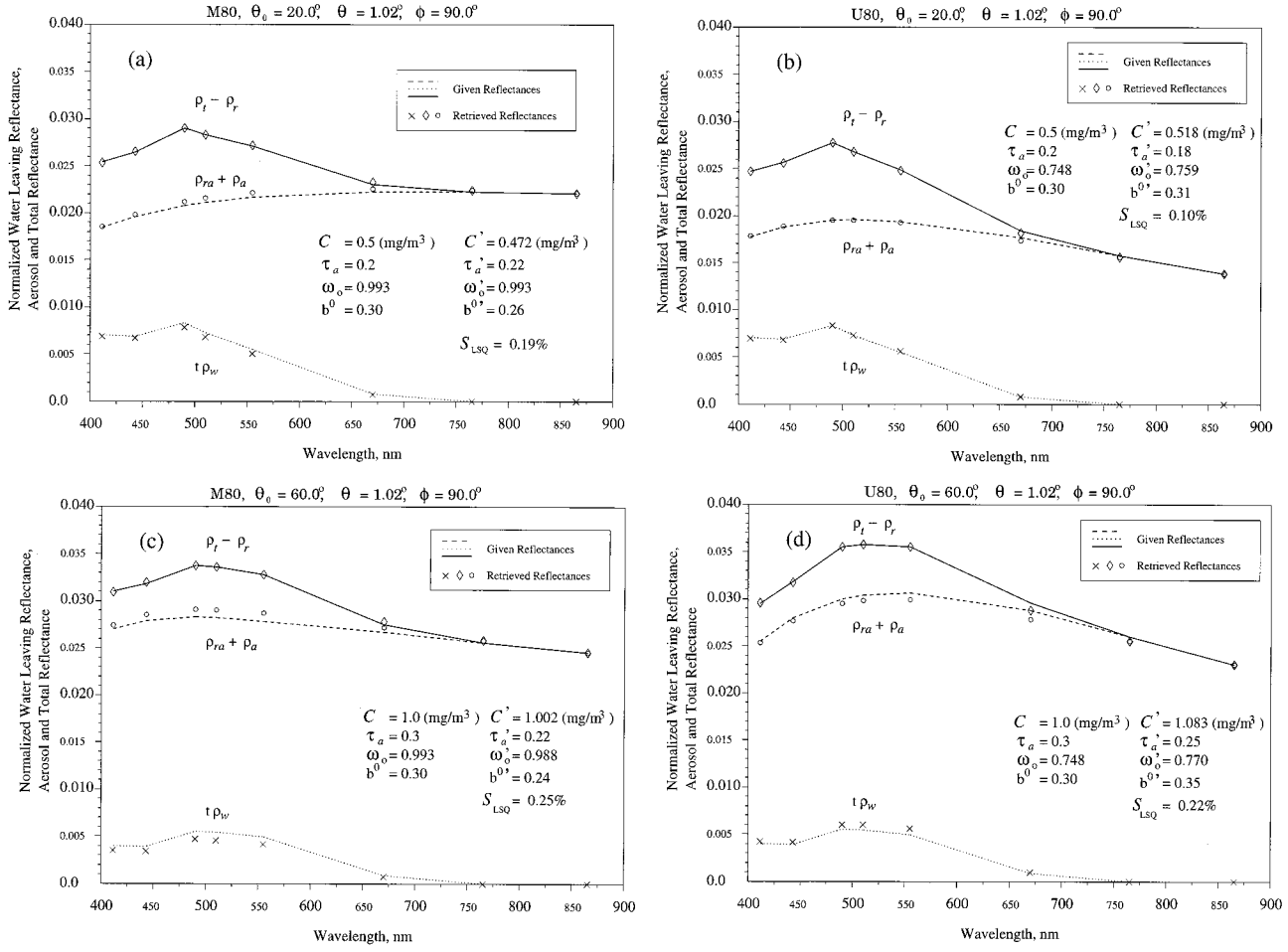

Fig. 4. Comparison between the given (curves) and the retrieved (symbols) reflectances by use of the Junge power-law size distribution for $\theta = 1.02°$ (i.e., near nadir): (a) M80 with $\theta_0 = 20°$, (b) U80 with $\theta_0 = 20°$, (c) M80 with $\theta_0 = 60°$, and (d) U80 with $\theta_0 = 60°$. Unprimed parameters are the true values; primed parameters are the retrieved values.

cellent, with an error at 443 nm less than 0.001 (recall that Gordon and Wang[9] used as a criterion for the performance of their SeaWiFS algorithm that the error in $t\rho_t$ at 443 nm should be smaller than ± 0.002). Retrievals of C, ω_0, and b^0 are also excellent. In contrast, the retrieval of $\tau_a(865)$ is sometimes poor, e.g., Figs. 4(c) and 4(d). This failure to derive acceptable values of $\tau_a(865)$ is completely explained by the fact that the scattering phase functions resulting from the Junge power-law distribution do not correspond well to those used in the generation of the pseudodata. Figures 5(a) and 5(b) compare the phase functions [$P(\Theta)$, where Θ is the scattering angle] derived in the retrievals, i.e., computed by use of the retrieved values of ν, m_i, and m_r, with those used in the generation of the pseudodata for Figs. 4(c) and 4(d), respectively. There are significant differences between the retrieved and true phase functions, and for the geometry in this situation (single-scattering angle $\Theta = 120°$) the difference causes the low values of $\tau_a(865)$ obtained by the algorithm.

Figure 6 provides similar results for pseudodata created with the T80 aerosol model. In this case the results are still acceptable, but not as good as those in Fig. 4. The degradation in this case is caused partially by the fact that the Junge power-law distribution cannot fit the T80 distribution well (Fig. 3) and partially by the fact that the optical thickness in the visible can become very large (Fig. 2) causing the reflectances to become very large [compare Fig. 6(b) with Figs. 4(c) and 4(d)]. In spite of the deficiencies of the algorithm, it is remarkable that in Figs. 4 and 6, the maximum error in the retrieved value of C is only slightly over 10%.

The performance of the algorithm for other geometries, pigment concentrations, and aerosol optical thicknesses is summarized in Tables 3–5. In these tables, the quantity being retrieved (ω_0, C, and b^0 for Tables 3, 4, and 5, respectively) is averaged over the seven Sun-viewing directions (Subsection 3.A), and its standard deviation (S_d) over the seven directions is also presented along with the error in the averaged quantity (D). A small value for S_d indicates stability in the performance as the Sun-viewing geometry is varied. Clearly, it is desirable for both S_d and D to be as small as possible.

The results for ω_0 at 865 nm (Table 3) show that weakly and strongly absorbing aerosols are well dis-

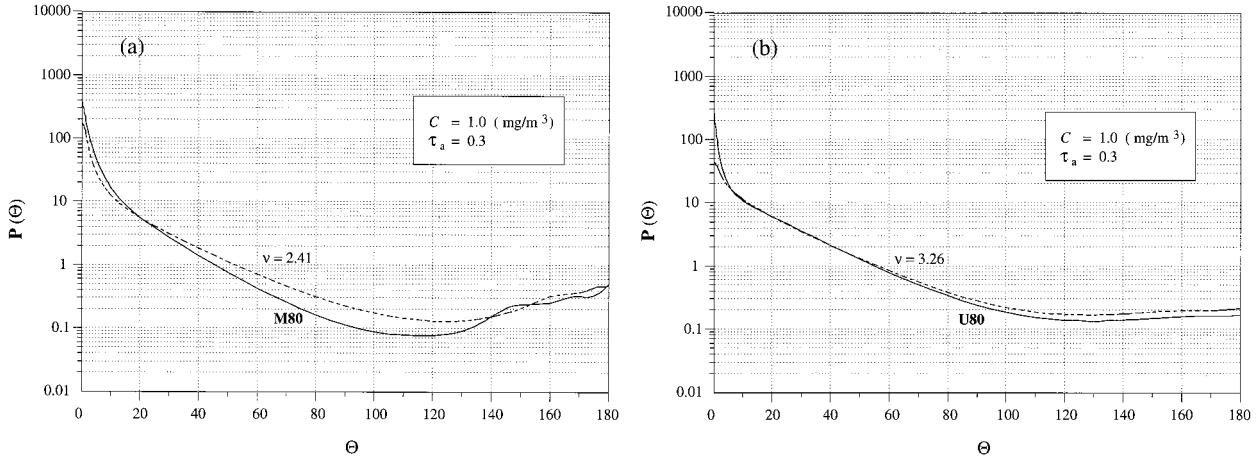

Fig. 5. Comparison of the true (solid curve) and retrieved (dashed curve) phase functions at 865 nm. The retrieved phase function is used to derive the aerosol optical thickness in Figs. 4(c) and 4(d): (a) M80 and (b) U80.

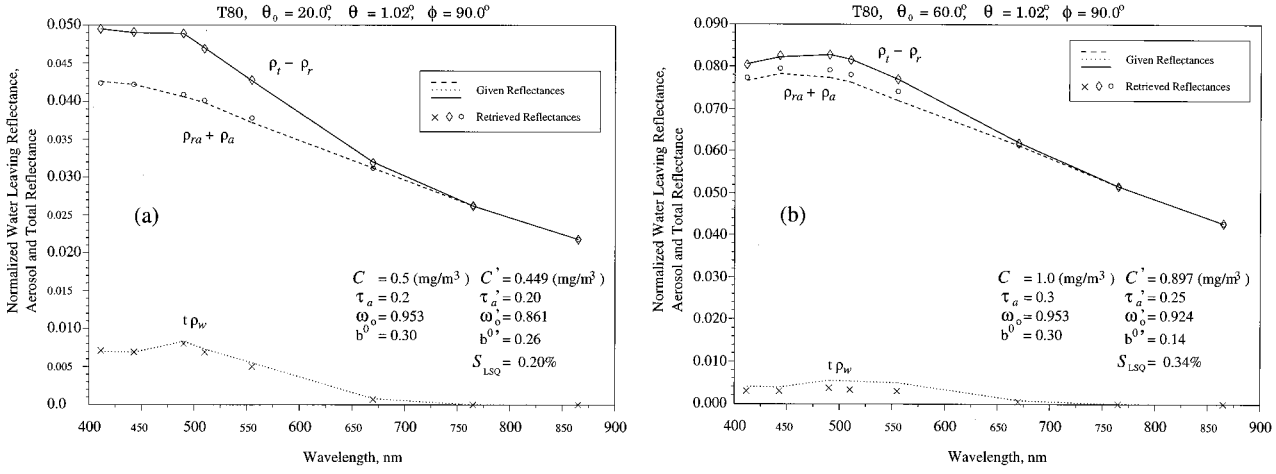

Fig. 6. Comparison between the given (curves) and the retrieved (symbols) reflectances by use of the Junge power-law size distribution for $\theta = 1.02°$ (i.e., near nadir): (a) T80 with $\theta_0 = 20°$ and (b) T80 with $\theta_0 = 60°$. Unprimed parameters are the true values; primed parameters are the retrieved values.

tinguished; however, the actual derived value of ω_0 is not as accurate as that obtained for the same test data by use of the Gordon *et al.*[11] algorithm (Table 2 in Ref. 11). In particular, larger errors are apparent for the weakly absorbing aerosols; however, the retrieval is generally improved as $\tau_a(865)$ increases, i.e., as the atmospheric contribution to ρ_t increases.

The retrievals of C (Table 4) are generally excellent, with the largest error being 17.6%. However, the T80 results are poorer than the others—the largest error in the absence of T80 being 10.4%. The error in C increases with increasing $\tau_a(865)$, but not dramatically. Other than a few T80 cases, S_d is generally <5%, indicating good stability with respect to Sun-viewing geometry. Table 5 shows that the retrieval of b^0 can usually be carried out with an error less than 20% (except for T80) with good Sun-viewing geometry stability.

We did not tabulate the performance regarding the retrievals of $\tau_a(865)$ as they are significantly poorer than those in Gordon *et al.*[11] because of the strong differences in the Shettle and Fenn[12] and the Junge power-law phase functions (Fig. 5).

The quality of the resulting fits of the optimized and TOA pseudoreflectances is measured by the value of S_{LSQ}. Table 6 provides the mean value of S_{LSQ} and its standard deviation σ_S over all values of $\tau_a(865)$ and C provided in Tables 3–5, as well as over all Sun-viewing geometries (a total of 63 individual determinations for each model used to generate the pseudodata). (The models UU80, U280, and U480 are described below.) The table shows that excellent fits are obtained with relatively low dispersion. As expected, the error is somewhat larger for the T80 case.

The results of this subsection suggest that the water parameters C and b^0 can be retrieved with reasonably good accuracy. The poorer results for ω_0 and, in particular, for $\tau_a(865)$ are simply manifestations of the fact that, as argued by Wang and Gordon,[27] an aerosol model that yields a phase function that correctly approximates the true phase function

Table 3. Retrieval of Aerosol's Single-Scattering Albedo[a]

		0.100			0.500			1.000		
	C (mg/m^3)	Result	S_d (%)	D (%)	Result	S_d (%)	D (%)	Result	S_d (%)	D (%)
M80	$\tau_a(865) = 0.10$	**0.938**	2.5	5.50	**0.968**	1.9	2.40	**0.972**	2.2	2.12
$\omega_0 = 0.993$	$\tau_a(865) = 0.20$	**0.954**	2.2	3.93	**0.971**	2.4	2.22	**0.974**	2.5	1.91
	$\tau_a(865) = 0.30$	**0.963**	1.8	3.02	**0.976**	1.9	1.22	**0.979**	2.0	1.41
C80	$\tau_a(865) = 0.10$	**0.943**	2.3	4.56	**0.970**	1.7	3.20	**0.972**	1.7	1.62
$\omega_0 = 0.988$	$\tau_a(865) = 0.20$	**0.960**	2.1	2.83	**0.977**	1.7	1.11	**0.979**	1.8	0.91
	$\tau_a(865) = 0.30$	**0.969**	1.9	1.92	**0.981**	1.6	0.71	**0.983**	1.5	0.51
T80	$\tau_a(865) = 0.10$	**0.842**	4.9	11.6	**0.867**	4.5	9.02	**0.872**	4.4	8.50
$\omega_0 = 0.953$	$\tau_a(865) = 0.20$	**0.877**	1.9	8.00	**0.891**	2.0	6.51	**0.892**	1.9	6.40
	$\tau_a(865) = 0.30$	**0.902**	1.6	5.35	**0.914**	1.0	4.09	**0.918**	1.0	3.67
U80	$\tau_a(865) = 0.10$	**0.744**	4.7	0.54	**0.745**	4.3	1.40	**0.745**	4.4	0.40
$\omega_0 = 0.748$	$\tau_a(865) = 0.20$	**0.770**	0.8	2.94	**0.769**	0.8	2.81	**0.770**	1.3	2.94
	$\tau_a(865) = 0.30$	**0.788**	1.7	5.35	**0.777**	1.2	3.88	**0.773**	1.5	3.34

[a]Tabulated are mean values of retrieved ω_0 for seven Sun-viewing geometries and each of four hypothetical atmospheric aerosols (M80, C80, T80, U80). Also provided are the standard deviations over viewing geometries divided by the mean (S_d) as well as the deviations from given parameters (D).

Table 4. Retrieval of Ocean's Pigment Concentration[a]

		0.100			0.500			1.000		
	C (mg/m^3)	Result	S_d (%)	D (%)	Result	S_d (%)	D (%)	Result	S_d (%)	D (%)
M80	$\tau_a(865) = 0.10$	**0.096**	1.8	4.00	**0.488**	1.8	2.40	**1.012**	1.1	1.20
$\omega_0 = 0.993$	$\tau_a(865) = 0.20$	**0.094**	2.9	6.00	**0.479**	3.7	4.20	**1.014**	2.3	1.40
	$\tau_a(865) = 0.30$	**0.093**	3.2	7.00	**0.473**	4.6	5.40	**1.010**	3.5	1.00
C80	$\tau_a(865) = 0.10$	**0.096**	2.1	4.00	**0.484**	2.1	3.20	**1.001**	1.9	0.10
$\omega_0 = 0.988$	$\tau_a(865) = 0.20$	**0.094**	3.2	6.00	**0.469**	1.7	6.20	**0.984**	4.3	1.60
	$\tau_a(865) = 0.30$	**0.093**	2.8	7.00	**0.459**	4.9	8.20	**0.959**	7.3	4.10
T80	$\tau_a(865) = 0.10$	**0.091**	4.9	9.00	**0.466**	4.0	6.80	**1.021**	6.1	2.10
$\omega_0 = 0.953$	$\tau_a(865) = 0.20$	**0.086**	1.9	14.0	**0.425**	9.9	15.0	**0.941**	7.0	5.90
	$\tau_a(865) = 0.30$	**0.090**	5.7	10.0	**0.412**	6.8	17.6	**0.874**	6.7	12.6
U80	$\tau_a(865) = 0.10$	**0.100**	0.8	0.00	**0.507**	0.7	1.40	**1.028**	1.9	2.80
$\omega_0 = 0.748$	$\tau_a(865) = 0.20$	**0.104**	1.4	4.00	**0.526**	2.7	5.20	**1.053**	3.2	5.30
	$\tau_a(865) = 0.30$	**0.110**	4.3	10.0	**0.552**	5.8	10.4	**1.070**	4.0	7.00

[a]Tabulated are mean values of retrieved C for seven Sun-viewing geometries and each of four hypothetical atmospheric aerosols (M80, C80, T80, U80). Also provided are the standard deviations over viewing geometries divided by the mean (S_d) as well as the deviations from given parameters (D).

Table 5. Retrieval of Water Scattering Parameter[a]

		0.100			0.500			1.000		
	C (mg/m^3)	Result	S_d (%)	D (%)	Result	S_d (%)	D (%)	Result	S_d (%)	D (%)
M80	$\tau_a(865) = 0.10$	**0.294**	1.1	2.00	**0.274**	4.1	8.67	**0.273**	4.4	3.20
$\omega_0 = 0.993$	$\tau_a(865) = 0.20$	**0.289**	1.7	3.67	**0.258**	7.3	14.0	**0.255**	8.2	15.0
	$\tau_a(865) = 0.30$	**0.286**	1.8	4.67	**0.249**	8.2	17.0	**0.246**	9.4	18.0
C80	$\tau_a(865) = 0.10$	**0.293**	1.6	2.33	**0.273**	4.9	3.20	**0.271**	5.3	9.67
$\omega_0 = 0.988$	$\tau_a(865) = 0.20$	**0.289**	2.2	3.67	**0.255**	8.0	15.0	**0.250**	9.0	16.7
	$\tau_a(865) = 0.30$	**0.287**	2.0	4.33	**0.247**	7.4	17.7	**0.239**	8.7	20.3
T80	$\tau_a(865) = 0.10$	**0.278**	6.5	7.33	**0.237**	18.0	21.0	**0.234**	19.0	22.0
$\omega_0 = 0.953$	$\tau_a(865) = 0.20$	**0.270**	6.4	10.0	**0.200**	23.0	33.3	**0.193**	23.7	36.0
	$\tau_a(865) = 0.30$	**0.288**	5.1	4.00	**0.201**	20.0	33.0	**0.186**	25.0	38.0
U80	$\tau_a(865) = 0.10$	**0.297**	1.0	1.00	**0.298**	1.8	0.67	**0.298**	1.7	0.67
$\omega_0 = 0.748$	$\tau_a(865) = 0.20$	**0.302**	0.5	0.67	**0.316**	1.9	5.33	**0.319**	2.4	6.33
	$\tau_a(865) = 0.30$	**0.311**	1.5	3.67	**0.350**	8.2	16.7	**0.354**	8.1	18.0

[a]Tabulated are mean values of retrieved b^0 for seven Sun-viewing geometries and each of four hypothetical atmospheric aerosols (M80, C80, T80, U80). Also provided are the standard deviations over viewing geometries divided by the mean (S_d) as well as the deviations from given parameters (D).

is required to retrieve accurate values, even for weakly absorbing aerosols. However, this is apparently not the case if the goal is to retrieve only the water parameters, i.e., a correct representation of the

Table 6. Mean S_{LSQ} and its Standard Deviation σ_S (both in %), over all Values of $\tau_a(865)$, C, and Sun-Viewing Geometries

Model	$\overline{S_{LSQ}}$	σ_S
M80	0.27	22
C80	0.28	19
T80	0.36	23
U80	0.15	16
U280	1.57	27
U480	5.58	27
UU80	133.48	68

Table 7. Values of the Residual Radiometric Calibration Uncertainty after Effecting an In-Orbit Calibration Adjustment[a]

λ_i (nm)	Uncertainty (%)
412	0.3
443	0.5
490	0.8
520	1.0
550	1.5
670	2.0
765	3.0
865	5.0

[a]From Ref. 28.

aerosol phase function is not necessary for retrieving water parameters.

SeaWiFS has an additional band at 670 nm that was not used in the results we presented in this subsection. The addition of this band in the optimization procedure did little to improve the retrievals, presumably because of its weak (but not negligible) response to changes in C and b^0.

C. Retrieval Results with Calibration Error in ρ_t

To illustrate the influence of radiometric calibration error on the performance of this algorithm, we follow Gordon *et al.*[11] and add error to ρ_t equal to the uncertainty expected after effecting an in-orbit calibration adjustment of the visible bands with respect to the band at λ_ℓ. Gordon[28] has shown that for such a

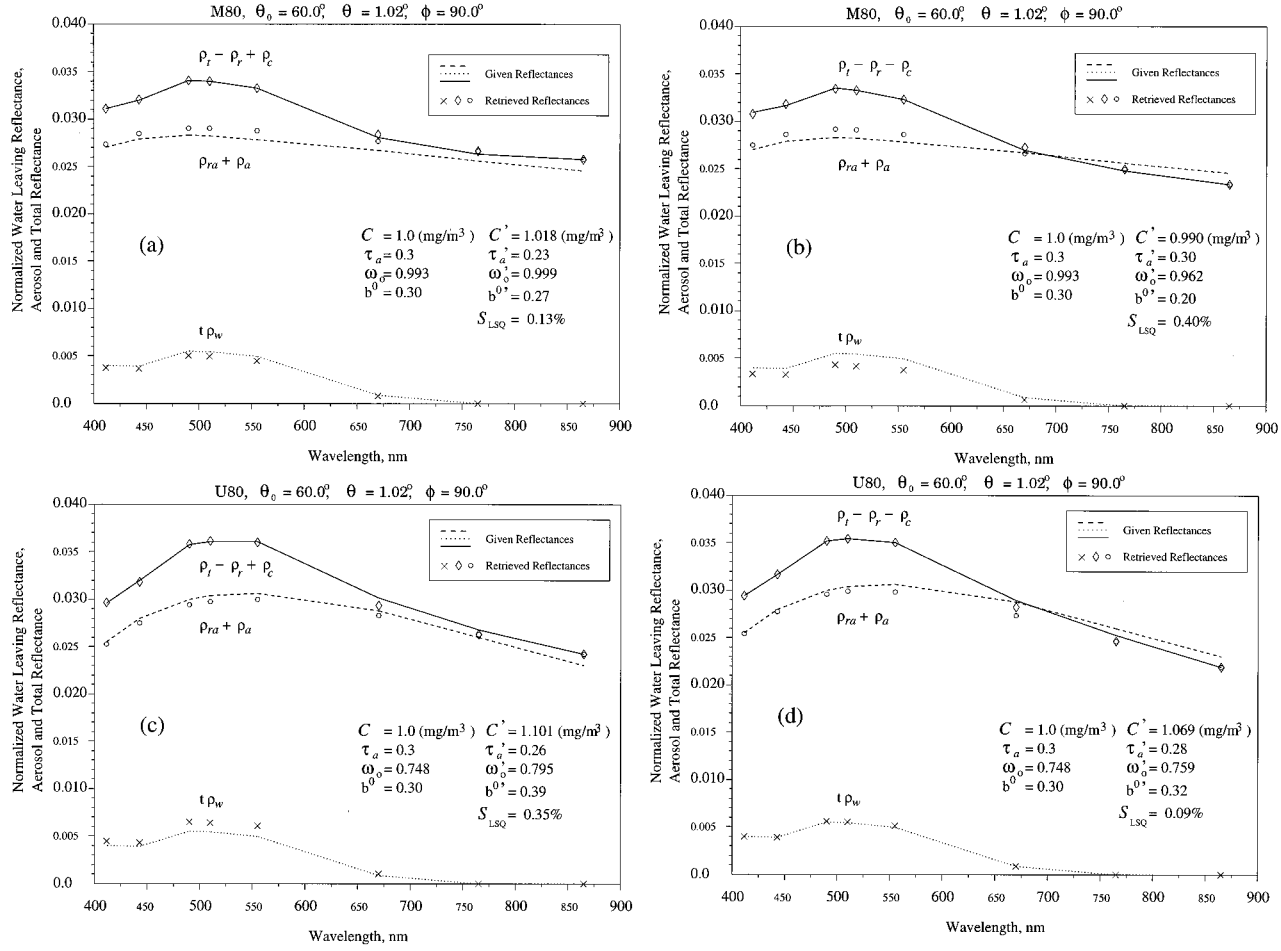

Fig. 7. Comparison between the given (curves) and the retrieved (symbols) reflectances by use of the Junge power-law size distribution for $\theta = 1.02°$ (i.e., near nadir) in the presence of the calibration errors in Table 7: (a) M80 with $\theta_0 = 60°$ and positive calibration error, (b) M80 with $\theta_0 = 60°$ and negative calibration error, (c) U80 with $\theta_0 = 60°$ and positive calibration error, and (d) U80 with $\theta_0 = 60°$ and negative calibration error. Unprimed parameters are the true values, primed parameters are the retrieved values, and ρ_c represents the calibration error.

Table 8. Retrieval of Ocean's Pigment Concentration with Negative Calibration Error[a]

		0.100			0.500			1.000		
	C (mg/m^3)	Result	S_d (%)	D (%)	Result	S_d (%)	D (%)	Result	S_d (%)	D (%)
M80	$\tau_a(865) = 0.10$	**0.094**	2.3	6.00	**0.479**	2.3	4.20	**1.004**	0.8	0.40
$\omega_0 = 0.993$	$\tau_a(865) = 0.20$	**0.091**	4.0	9.00	**0.463**	4.6	7.40	**1.005**	2.2	0.50
	$\tau_a(865) = 0.30$	**0.090**	4.7	3.00	**0.452**	6.1	9.60	**0.998**	4.0	0.20
C80	$\tau_a(865) = 0.10$	**0.094**	2.6	6.00	**0.476**	2.5	4.80	**0.997**	0.9	0.30
$\omega_0 = 0.988$	$\tau_a(865) = 0.20$	**0.090**	4.7	10.0	**0.455**	5.2	9.00	**0.983**	2.2	1.70
	$\tau_a(865) = 0.30$	**0.088**	5.3	12.0	**0.438**	6.5	12.4	**0.964**	4.4	3.60
T80	$\tau_a(865) = 0.10$	**0.086**	10.0	5.00	**0.437**	9.5	12.6	**1.038**	14.0	3.80
$\omega_0 = 0.953$	$\tau_a(865) = 0.20$	**0.078**	14.0	22.0	**0.377**	19.0	24.6	**0.836**	3.4	16.4
	$\tau_a(865) = 0.30$	**0.081**	12.0	19.0	**0.337**	15.0	32.6	**0.640**	26.0	36.0
U80	$\tau_a(865) = 0.10$	**0.098**	1.5	2.00	**0.496**	0.2	0.80	**1.021**	2.7	2.10
$\omega_0 = 0.748$	$\tau_a(865) = 0.20$	**0.099**	2.7	1.00	**0.507**	1.9	1.40	**1.033**	3.5	3.30
	$\tau_a(865) = 0.30$	**0.104**	3.2	4.0	**0.530**	4.7	6.00	**1.056**	4.1	5.60

[a]Tabulated are mean values of retrieved C for seven Sun-viewing geometries and each of four hypothetical atmospheric aerosols (M80, C80, T80, U80). Also provided are the standard deviations over viewing geometries divided by the mean (S_d) as well as the deviations from given parameters (D).

procedure, the residual calibration error in all the bands will have the same sign as that at λ_ℓ, and the magnitude of the error will progressively decrease into the visible, roughly as ρ_r increases. Table 7 provides the estimated residual uncertainty (in percent) given an uncertainty of 5% in the radiometry at λ_ℓ. We added (subtracted) the error in Table 7 to (from) the pseudodata used in Subsection 3.B to produce erroneous reflectances. The algorithm was then operated by use of these reflectances as input pseudodata. Figure 7 provides examples of the retrievals in the presence of these errors. It shows that the retrieval of $\rho_a + \rho_{ra}$ is too large (small) if the radiometric error is positive (negative). Typically, this is compensated by the opposite behavior in $t\rho_w$. To achieve this, the algorithm apparently varies b^0 holding C to the nearly correct value [compare Figs. 7(a) and 7(b) with Fig. 4(c), and Figs. 7(c) and 7(d) with Fig. 4(d)]. Note that the calibration error will cause an incorrect ν to be chosen: A positive (negative) error results in a smaller (larger) ν. The quality of the fits is only marginally degraded from the error-free case. Averaging $\overline{S_{\mathrm{LSQ}}}$ for the M80, C80, T80, and U80 in Table 6 yields 0.26%. This is increased only to 0.37% for a negative calibration error (the worse case of the two).

Tables 8 and 9 summarize all the retrievals in the presence of radiometric calibration error. They should be compared with Table 4. Although there are some systematic variations in C with calibration error, e.g., for $C = 0.1$ mg/m^3 the retrieved C tends to be larger (smaller) for a positive (negative) calibration error, it is not systematic over the range of C values or aerosol models. We can conclude from this analysis that the algorithm is relatively insensitive to radiometric calibration error of the magnitude expected after in-orbit calibration adjustment. It is certainly no more sensitive than the Gordon *et al.*[11] algorithm.

Table 9. Retrieval of Ocean's Pigment Concentration with Positive Calibration Error[a]

		0.100			0.500			1.000		
	C (mg/m^3)	Result	S_d (%)	D (%)	Result	S_d (%)	D (%)	Result	S_d (%)	D (%)
M80	$\tau_a(865) = 0.10$	**0.098**	1.6	2.00	**0.494**	2.7	1.20	**1.011**	4.2	1.10
$\omega_0 = 0.993$	$\tau_a(865) = 0.20$	**0.097**	2.2	3.00	**0.487**	5.0	2.60	**0.999**	8.5	0.10
	$\tau_a(865) = 0.30$	**0.097**	2.2	3.00	**0.485**	6.2	3.00	**0.991**	11.0	0.90
C80	$\tau_a(865) = 0.10$	**0.098**	1.6	2.00	**0.490**	3.6	2.00	**0.995**	6.3	0.50
$\omega_0 = 0.988$	$\tau_a(865) = 0.20$	**0.097**	2.2	3.00	**0.478**	7.1	4.40	**0.966**	12.0	3.40
	$\tau_a(865) = 0.30$	**0.097**	2.6	3.00	**0.471**	10.0	5.80	**0.940**	17.0	6.00
T80	$\tau_a(865) = 0.10$	**0.095**	4.7	5.00	**0.487**	2.4	2.60	**1.037**	4.9	3.70
$\omega_0 = 0.953$	$\tau_a(865) = 0.20$	**0.093**	1.3	7.00	**0.470**	4.0	6.00	**0.935**	3.0	6.50
	$\tau_a(865) = 0.30$	**0.096**	4.4	4.0	**0.469**	2.1	6.20	**0.943**	2.7	5.70
U80	$\tau_a(865) = 0.10$	**0.103**	0.8	3.00	**0.519**	1.1	3.80	**1.043**	2.3	4.30
$\omega_0 = 0.748$	$\tau_a(865) = 0.20$	**0.109**	2.8	9.00	**0.543**	3.8	8.60	**1.062**	2.9	6.20
	$\tau_a(865) = 0.30$	**0.116**	5.7	16.0	**0.573**	6.4	14.6	**1.089**	3.6	8.90

[a]Tabulated are mean values of retrieved C for seven Sun-viewing geometries and each of four hypothetical atmospheric aerosols (M80, C80, T80, U80). Also provided are the standard deviations over viewing geometries divided by the mean (S_d) as well as the deviations from given parameters (D).

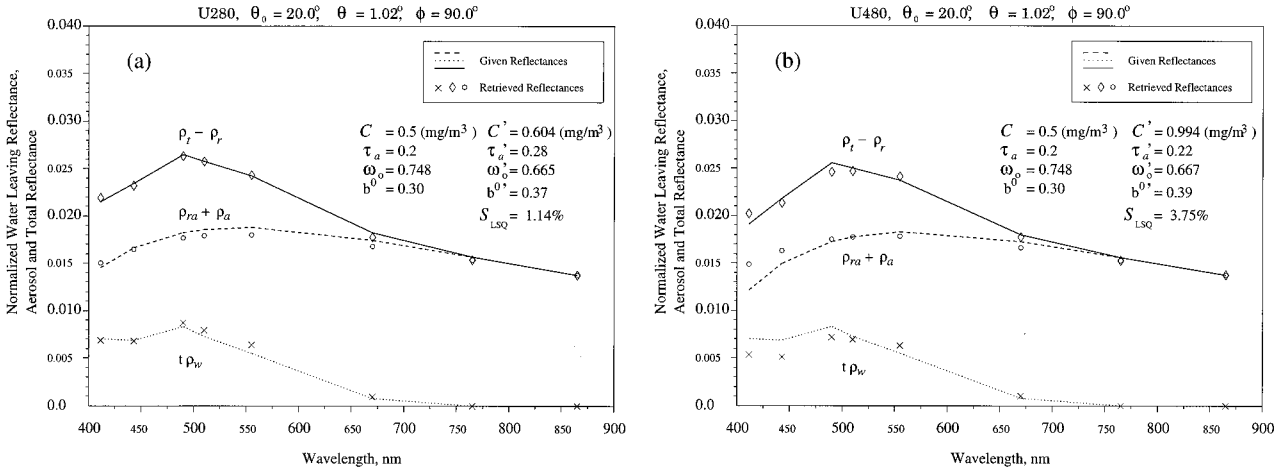

Fig. 8. Comparison between the given (curves) and the retrieved (symbols) reflectances by use of the Junge power-law size distribution for $\theta_0 = 20°$ and $\theta = 1.02°$ (i.e., near nadir) for cases in which the aerosol is uniformly mixed with air from the surface to an altitude h: (a) U80 aerosol with $h = 2$ km (U280) and (b) U80 aerosol with $h = 4$ km (U480). Unprimed parameters are the true values; primed parameters are the retrieved values.

D. Influence of Aerosol Vertical Structure on Retrieval of *C*

In the results described in Subsections 3.B and 3.C, it was assumed that the aerosol is located in a thin layer near the sea surface, as it was shown that the vertical structure of the aerosol concentration is irrelevant as long as the aerosol is weakly absorbing.[10] However, when the aerosol is strongly absorbing, this is not the case.[10,11] In the above subsections, the vertical structure of the test pseudodata and the candidate Junge power-law models were identical. In this subsection, we examine the quality of the retrievals when the urban aerosol is uniformly mixed with air (molecular scattering) from the surface to 2 km (U280), from the surface to 4 km (U480), and uniformly mixed with air from the surface to the TOA (UU80). In contrast, the radiative transfer computations for the candidate aerosol models still employ a two-layer atmosphere with all aerosol scattering in the lower layer and all molecular scattering in the upper layer.

Figure 8 provides examples of the performance of the algorithm for the U280 and U480 cases with $\theta_0 = 20°$ and $\theta = 1.02°$. These figures should be compared with Fig. 4(b) for which the pseudodata and the candidate models have the same vertical distribution of aerosol. Note the decreasing quality of the retrievals as the aerosol layer thickens. This is also manifest in a decreasing quality of the fit of the computed reflectances to the pseudodata, i.e., increasing S_{LSQ}, with increased layer thickness (Table 6). Table 10 provides a summary comparing the retrieved C, averaged over Sun-viewing geometry, for the U280 and U480 with that for U80. The UU80 retrievals are not shown because the maximum value of C allowed (1.5 mg/m^3) was always chosen. Note that as the layer thickens, the retrieved values for C increase. This is explained as follows. Increasing the layer thickness causes $\rho_a(\lambda) + \rho_{ra}(\lambda)$ to become increasing smaller as λ decreases (see Fig. 4 of Ref. 11). The algorithm tries to cope with this decrease in absorption by (1) choosing the largest value of m_i available and (2) increasing C to further reduce $\rho_t(\lambda) - \rho_r(\lambda)$ in the blue relative to the red. The fact that the U280 retrievals were realistic is encouraging. It

Table 10. Retrieval of Ocean's Pigment Concentration[a]

		0.100			0.500			1.000		
	C (mg/m^3)	Result	S_d (%)	D (%)	Result	S_d (%)	D (%)	Result	S_d (%)	D (%)
U80	$\tau_a(865) = 0.10$	**0.100**	0.8	0.00	**0.507**	0.7	1.40	**1.028**	1.9	2.80
$\omega_0 = 0.748$	$\tau_a(865) = 0.20$	**0.104**	1.4	4.00	**0.526**	2.7	5.20	**1.053**	3.2	5.30
	$\tau_a(865) = 0.30$	**0.110**	4.3	10.0	**0.552**	5.8	10.4	**1.070**	4.0	7.00
U280	$\tau_a(865) = 0.10$	**0.110**	2.8	10.0	**0.602**	9.8	20.4	**1.305**	11.0	30.5
$\omega_0 = 0.748$	$\tau_a(865) = 0.20$	**0.122**	6.3	22.0	**0.575**	3.0	15.0	**1.120**	7.9	12.0
	$\tau_a(865) = 0.30$	**0.138**	12.0	38.0	**0.631**	16.0	26.2	**0.959**	8.6	4.10
U480	$\tau_a(865) = 0.10$	**0.120**	6.7	20.0	**0.941**	28.0	88.2	**1.500**	0.0	50.0
$\omega_0 = 0.748$	$\tau_a(865) = 0.20$	**0.142**	14.0	42.0	**1.198**	19.0	140.0	**1.500**	0.0	50.0
	$\tau_a(865) = 0.30$	**0.172**	25.0	72.0	**1.084**	13.0	102.0	**1.500**	0.0	50.0

[a]Tabulated are mean values of retrieved C for seven Sun-viewing geometries and each of four hypothetical atmospheric aerosols (M80, C80, T80, U80. Also provided are the standard deviations over viewing geometries divided by the mean (S_d) as well as the deviations from given parameters (D).

suggests that the algorithm as presented could handle aerosol vertical structure with only minor changes. The reasoning is as follows. First, as most strongly absorbing aerosols, e.g., wind-blown dust, smoke from biomass burning, etc., are likely to be mixed to altitudes of 2–4 km, it is clear that the simple vertical structure of the atmosphere used in generating the candidate model LUT's (a two-layer model: all aerosol scattering in the lower layer and all molecular scattering in the upper layer) must be modified. Second, because the vertical structure in the case of nonabsorbing or weakly absorbing aerosols is irrelevant, use of LUT's with aerosol mixed higher in the atmosphere will not have a negative impact on the retrieval of C for such aerosols (M80, C80, and T80). Third, the U280 retrievals were good even though the vertical distribution of the aerosol mixing was in error by 2 km. These observations suggest that if the candidate LUT's were all generated for an aerosol mixed to 2 km, the performance in the case of the M80, C80, T80, and U80 examples would be only slightly degraded from that in Table 4, whereas the performance for U480 would be significantly improved over that in Table 10 and that for U280 would be slightly improved. This is the strategy that is used in implementing the algorithm.

4. Discussion

The results in this paper are in agreement with the conclusion of Zhao and Nakajima[14]: The Junge power-law aerosol size distribution can be usefully applied to the problem of atmospheric correction of ocean color sensors. However, we have extended their algorithm, in which only a single value of refractive index (1.50–i0.01) was used for both the Junge power-law distribution and the test pseudodata to allow both m_r and m_i to be determined in the nonlinear optimization procedure. Simulations show that our algorithm yields excellent retrievals of C in atmospheres with either weakly or strongly absorbing aerosols, but retrieval of the aerosol optical thickness can show large error. The error in $\tau_a(865)$ is traced to significant differences between the phase functions of the optimized Junge power-law and the test pseudodata (Fig. 5). In contrast, Zhao and Nakajima typically obtained excellent $\tau_a(550)$ retrievals (error ~10%). This discrepancy is probably due to the fact that they used the same refractive index for all their computations. Hansen and Travis[16] show that for a fixed refractive index, the phase functions computed for significantly different size distributions can be similar as long as the size distributions have the same effective radius and effective variance. In our more realistic simulations, in which even the individual components of the log-normal size distributions for the test data [Eqs. (8) and (9)] have different refractive indices (which also depend on λ), this similarity is precluded, preventing an accurate estimate of $\tau_a(865)$.

Our results suggest that the detailed shape of the aerosol-scattering phase function is not relevant to atmospheric correction in case 1 waters, i.e., we can retrieve excellent values of C (Fig. 4) with poor phase functions (Fig. 5). Apparently, the most important parameters are ω_0 and the spectral variation of optical thickness, $\tau_a(\lambda)/\tau_a(865)$. [Note that the absolute value of $\tau_a(865)$ is directly dependent on the phase function that is not relevant.] Gordon[10] has already pointed out that the choice of candidate aerosol models in the Gordon and Wang[9] correction algorithm forces a particular $\omega_0 - \tau_a(\lambda)/\tau_a(865)$ relationship to be applied in the correction. In the present algorithm, no such relationship is impressed on the retrievals—ω_0 is determined mostly by ν and m_i, and $\tau_a(\lambda)/\tau_a(865)$ is principally determined by ν.

The fact that excellent retrievals of C are obtained even though the phase function of the resulting aerosol model is a poor approximation to the true phase function (Fig. 5) suggests that this algorithm is not limited by the fact that the aerosol optical properties [ω_0, $\tau_a(\lambda)/\tau_a(865)$, and $P(\Theta)$] are computed assuming that the aerosol consists of homogeneous spheres (Mie theory). Mishchenko and co-workers[29,30] have shown that, in the case of randomly oriented spheroids used as a model for dustlike tropospheric aerosols, the only aerosol optical property that is strongly influenced by the particle shape is the phase function. Thus, for the purpose of retrieving C, the use of Mie theory should not restrict the applicability of the algorithm. In contrast, the retrieved $\tau_a(865)$ depends directly on $P(\Theta)$ and therefore will only be correct if $P(\Theta)$ is correct.[27]

We have made the implicit assumption that m_i and m_r are constant for the Junge power-law models. This results in only a small variation in ω_0 with λ (Table 2). Unfortunately, some aerosol species, such as wind-blown dust, are colored and show significant variation in m_i (and therefore ω_0) with wavelength.[31] The algorithm as described above cannot handle these aerosols; however, with minor changes it should be able to. Essentially, all that is needed is to force a prescribed spectral variation in m_r and m_i—which, along with ν and $\tau_a(865)$ determined as in Subsection 3.A, fixes all the aerosol properties—and vary only C and b^0 until a minimum in S_{LSQ} is reached. If the correct spectral variation in m_r and m_i is chosen, the minimal S_{LSQ} in this case should be considerably smaller than that obtained by use of the wavelength-independent values of m_r and m_i. Thus a larger than expected minimal S_{LSQ} could be employed as a signal that colored aerosols may be present and that a set of variable m values should be tested to see if S_{LSQ} can be reduced.

Our proposed method for dealing with the vertical distribution of strongly absorbing aerosols—placing them in a uniformly mixed layer with a thickness of 2 km in the computations used to generate the Junge power-law LUT's—may not be optimum. Unfortunately, other approaches, such as trying to retrieve the layer thickness by use of LUT's generated for several-layer thicknesses,[11] may require too much computer memory to be useful. There were 72 separate aerosol models already used as the basis for our interpolation of $\rho_a + \rho_{ra}$ for arbitrary ν, m_r, and m_i. These require

approximately 500 Mbytes of random access memory to operate the algorithm. Nevertheless, in the final analysis all atmospheric correction procedures must compromise in some manner to deal with the problem of absorbing aerosol vertical structure.

We believe that the principal advantage of the present algorithm over and above that proposed by Gordon *et al.*[11] is the fact that realistic multicomponent aerosol models are not required for the extraction of ocean properties (although the spectral variation of m will be required for colored aerosols). Unfortunately, by abandoning realistic models in favor of the simpler Junge power law, we lose some ability to retrieve meaningful aerosol properties, e.g., $\tau_a(865)$.

We are currently studying ways of making this algorithm more efficient, with the goal that it can be applied to the processing of SeaWiFS and MODIS imagery.

The authors are grateful for support from the National Aeronautics and Space Administration, Goddard Space Flight Center, under contracts NAS5-31363 and NAS5-31734.

References

1. H. R. Gordon, D. K. Clark, J. L. Mueller, and W. A. Hovis, "Phytoplankton pigments derived from the Nimbus-7 CZCS: initial comparisons with surface measurements," Science **210,** 63–66 (1980).
2. W. A. Hovis, D. K. Clark, F. Anderson, R. W. Austin, W. H. Wilson, E. T. Baker, D. Ball, H. R. Gordon, J. L. Mueller, S. Y. E. Sayed, B. Strum, R. C. Wrigley, and C. S. Yentsch, "Nimbus 7 coastal zone color scanner: system description and initial imagery," Science **210,** 60–63 (1980).
3. H. R. Gordon and A. Y. Morel, *Remote Assessment of Ocean Color for Interpretation of Satellite Visible Imagery: a Review* (Springer-Verlag, New York, 1983).
4. S. B. Hooker, W. E. Esaias, G. C. Feldman, W. W. Gregg, and C. R. McClain, "SeaWiFS Technical Report Series: an Overview of SeaWiFS and Ocean Color," NASA Tech. Memo. 104566 (NASA, Greenbelt, Md., 1992), Vol. 1.
5. V. V. Salomonson, W. L. Barnes, P. W. Maymon, H. E. Montgomery, and H. Ostrow, "MODIS: advanced facility instrument for studies of the earth as a system," IEEE Geosci. Remote Sensing **27,** 145–152 (1989).
6. H. R. Gordon, "Radiative transfer: a technique for simulating the ocean in satellite remote sensing calculations," Appl. Opt. **15,** 1974–1979 (1976).
7. H. R. Gordon, "Removal of atmospheric effects from satellite imagery of the oceans," Appl. Opt. **17,** 1631–1636 (1978).
8. H. R. Gordon, D. K. Clark, J. W. Brown, O. B. Brown, R. H. Evans, and W. W. Broenkow, "Phytoplankton pigment concentrations in the Middle Atlantic Bight: comparison between ship determinations and Coastal Zone Color Scanner estimates," Appl. Opt. **22,** 20–36 (1983).
9. H. R. Gordon and M. Wang, "Retrieval of water-leaving radiance and aerosol optical thickness over the oceans with SeaWiFS: a preliminary algorithm," Appl. Opt. **33,** 443–452 (1994).
10. H. R. Gordon, "Atmospheric correction of ocean color imagery in the earth observing system era," J. Geophys. Res. D **102,** 17,081–17,106 (1997).
11. H. R. Gordon, T. Du, and T. Zhang, "Remote sensing of ocean color and aerosol properties: resolving the issue of aerosol absorption," Appl. Opt. **36,** 8670–8684 (1997).
12. E. P. Shettle and R. W. Fenn, "Models for the aerosols of the lower atmosphere and the effects of humidity variations on their optical properties," AFGL-TR-79-0214 (U.S. Air Force Geophysics Laboratory, Hanscomb Airforce Base, Mass., 1979).
13. H. R. Gordon, O. B. Brown, R. H. Evans, J. W. Brown, R. C. Smith, K. S. Baker, and D. K. Clark, "A semi-analytic radiance model of ocean color," J. Geophys. Res. D **93,** 10,909–10,924 (1988).
14. F. Zhao and T. Nakajima, "Simultaneous determination of water-leaving reflectance and aerosol optical thickness from Coastal Zone Color Scanner measurements," Appl. Opt. **36,** 6949–6956 (1997).
15. C. Junge, "Atmospheric chemistry," Adv. Geophys. **4,** 1–108 (1958).
16. J. E. Hansen and L. D. Travis, "Light scattering in planetary atmospheres," Space Sci. Rev. **16,** 527–610 (1974).
17. H. R. Gordon, J. W. Brown, and R. H. Evans, "Exact Rayleigh scattering calculations for use with the Nimbus-7 Coastal Zone Color Scanner," Appl. Opt. **27,** 862–871 (1988).
18. A. Morel and B. Gentili, "Diffuse reflectance of oceanic waters: its dependence on Sun angle as influenced by the molecular scattering contribution," Appl. Opt. **30,** 4427–4438 (1991).
19. A. Morel and B. Gentili, "Diffuse reflectance of oceanic waters. II. Bidirectional aspects," Appl. Opt. **32,** 6864–6879 (1993).
20. A. Morel, K. J. Voss, and B. Gentili, "Bidirectional reflectance of oceanic waters: a comparison of modeled and measured upward radiance fields," J. Geophys. Res. C **100,** 13,143–13,150 (1995).
21. A. Morel and B. Gentili, "Diffuse reflectance of oceanic waters. III. Implication of bidirectionality for the remote sensing problem," Appl. Opt. **35,** 4850–4862 (1996).
22. M. Abramowitz and I. A. Stegun, eds., *Handbook of Mathematical Functions* (Dover, New York, 1970).
23. R. Fletcher, *Practical Methods of Optimization* (Wiley, New York, 1980), Vols. 1 and 2.
24. P. E. Gill and W. Murray, "Quasi-Newton methods for unconstrained optimization," J. Inst. Maths. Its Appl. **9,** 91–108 (1972).
25. M. J. D. Powell, "Some global convergence properties of a variable metric algorithm for minimization without exact line searches," AERE Harwell Rep. CSS15 (Atomic Energy Research Establishment, Harwell, Oxfordshire, UK, 1975).
26. International Mathematical & Statistical Library, *Reference Manual* (IMSL Inc., Houston, Texas, 1982), Vol. 4.
27. M. Wang and H. R. Gordon, "Estimating aerosol optical properties over the oceans with the multiangle imaging spectroradiometer: some preliminary studies," Appl. Opt. **33,** 4042–4057 (1994).
28. H. R. Gordon, "In-orbit calibration strategy for ocean color sensors," Remote Sensing Environ. **63,** 265–278 (1998).
29. M. I. Mishchenko and L. D. Travis, "Light scattering by polydispersions of randomly oriented spheroids with sizes comparable to wavelengths of observation," Appl. Opt. **33,** 7206–7225 (1994).
30. M. I. Mishchenko, L. D. Travis, R. A. Kahn, and R. A. West, "Modeling phase functions for dustlike tropospheric aerosols using a shape mixture of randomly oriented spheroids," J. Geophys. Res. D **102,** 16,831–16,847 (1997).
31. G. A. d'Almeida, P. Koepke, and E. P. Shettle, *Atmospheric Aerosols—Global Climatology and Radiative Characteristics* (Deepak, Hampton, Va., 1991).